Nanoscale Electrokinetics and Microvortices: How Microhydrodynamics Affects Nanofluidic Ion Flux

Hsueh-Chia Chang,[1] Gilad Yossifon,[2] and Evgeny A. Demekhin[3]

[1] Department of Chemical and Biomolecular Engineering, Center for Microfluidics and Medical Diagnostics, University of Notre Dame, Notre Dame, Indiana 46556; email: hchang@nd.edu

[2] Faculty of Mechanical Engineering, Micro- and Nanofluidics Laboratory, Technion – Israel Institute of Technology, Technion City 32000, Israel; email: yossifon@tx.technion.ac.il

[3] Department of Computational Mathematics and Computer Science, Kuban State University, Krasnodar 350040, Russia; email: edemekhi@gmail.com

Keywords

overlimiting current, nanoslot ion current, extended polarization, depletion front, rectification

Abstract

When a direct current (DC) electric field is applied across an ion-selective nanoporous membrane or a nanochannel with an overlapping Debye layer, a surprising microvortex instability occurs on the side of the membrane/channel through which counterions enter. Despite its micro and nano length scales, this instability exhibits all the hallmarks of other classical hydrodynamic instabilities—a subharmonic cascade, a wide-band fluctuation spectrum, and a coherent-structure dominated by spatiotemporal dynamics. Moreover, the resulting convection enhances the ion flux into the ion-selective medium and gives rise to an overlimiting-current bifurcation in the current-voltage relationship. This hydrodynamically driven nonequilibrium ion flux does not seem to have any equivalent in cell membrane ion channels. Yet, by introducing asymmetric entrances to provide different polarized regions and/or viscous arrest of the vortex instability, one can fabricate a hydrodynamic nanofluidic diode. With other modifications, hysteretic, excitable, and oscillatory ion flux dynamics could also be elicited—all with strong hydrodynamic features.

INTRODUCTION

The advent of nanofabrication technologies in the past decade has spurred numerous new and active research areas. These areas include molecular Raman scattering enhanced by plasmonic resonance at metallic nanocolloids and at hotspots on nanoscale grids, near-field subwavelength single-molecule imaging by nanoscale conic structures, the enhancement of solar-cell efficiency by nanostructure scattering, and field-effect transistor molecular sensors consisting of single carbon nanotubes.

In fluid mechanics, whether the thermal conductivity of a suspension of nanocolloids (nanofluids) is anomalously high (Eastman et al. 2001) has been hotly debated for several years. In another and larger nanofluidic community, our ability to fabricate pores or channels with spatial dimensions comparable with ion channels on cell membranes has generated considerable excitement. There are dreams, mostly unrealized, that we can fabricate channels that mimic ion channels, such that they allow only certain ions/molecules to pass and can elicit the rich electrical action potential dynamics of a cell that is typically attributed to ion channels: excitability, bistability, and oscillations (Keener & Sneyd 1998). The gating property could be steric, electrostatic, or endowed by specific gating molecules functionalized to the nanochannel entrance. In fact, single-molecule translocation through a nanopore can now be detected (Craighead 2006, Dekker 2007) by conductance or impedance measurement across the pore and can be directly visualized (Mannion & Craighead 2006). While translocating through a nanopore, a large linear molecule typically assumes an elongated conformation, thus suggesting that impedance measurement by interdigitated nanoelectrodes within the pore can decipher the identity of each base of a double-stranded DNA—a rapid, next-generation sequencing technique that IBM and others are currently pursuing (Branton et al. 2008).

Because the electric field of the surface charge within such nanochannels spans the entire channel (the Debye layers of opposite walls overlap), the nanochannel can regulate electrophoretic ion flux through it (ion permselectivity) (Stein et al. 2004). There are hence hopes that we can produce new integrated nanofluidic ion circuits with rectification (diode) (Vlassiouk & Siwy 2007), gating (transistor) (Karnik et al. 2005, Cheng & Guo 2007), and nonlinear *I-V* (current-voltage) characteristics (Kim et al. 2008). These nanofluidic circuits would be the analogs of positively (P) and negatively (N) doped semiconductors, with surface charges replacing the doped impurities and counter-/coions replacing the holes and electrons. Just as P and N semiconductors have been integrated into PN junctions and integrated electronic circuits for various devices, the analogous nanofluidic ion circuits can be used for several molecular/ion sensing, reaction, and energy-conversion applications: to amplify molecular sensing signals (Chang & Yossifon 2009), concentrate analytes (Pu et al. 2004, Wang et al. 2008), control the local reactant environment (Cheng et al. 2010), or even precondition electrochemical (electron-transfer) reactions (Basuray et al. 2009) for molecular assays and enhance electrical energy conversion from mechanical energies (Heyden et al. 2005). These circuits need not be artificial nanochannels—they can also be nanoporous membranes with similar ion-flux regulation properties. Some of these nanopore circuits have been realized and integrated into microfluidic devices (Chang & Yeo 2010). For example, **Figure 1** shows hysteretic and rectification measurements by Li-Jing Cheng at University of Michigan (Cheng & Guo 2009) and at Notre Dame for a single nanopore with asymmetric surface charges and for bipolar membranes that can break water. As in diodes, an asymmetric PN junction is responsible for rectification, whereas the ion-generation mechanism of the water-breaking reaction is responsible for hysteresis. The bipolar membrane is part of a microfluidic device for on-chip protein separation by isoelectric focusing.

In this review, we focus on an often-ignored phenomenon in nanoscale ion flux: hydrodynamics. At first glance, nanoscale hydrodynamics should contribute negligibly to ion flux, given the
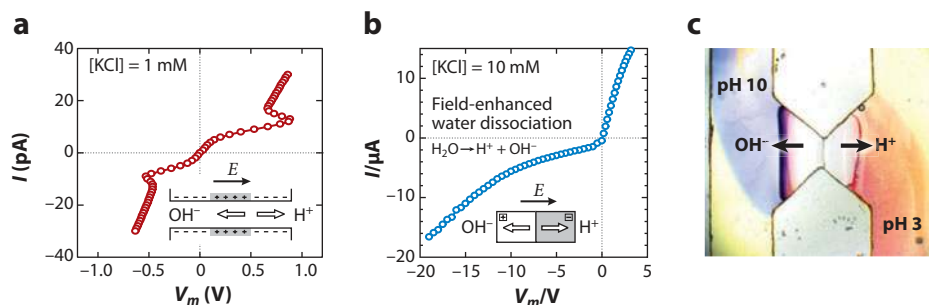
Figure 1

Field-enhanced water dissociation increases ionic currents in (*a*) a reverse-biased 20-nm-thick bipolar-junction nanofluidic channel containing positive and negative surface charges ($|V_m| > 0.6$ V) and (*b*) a UV-polymerized bipolar membrane ($V_m < -10$ V). (*c*) Hydroxide ions and protons are produced at the bipolar membrane junction and transport to opposite sides of the membrane. The pH change of the solution in the microchannels can be observed with a mixture of a universal pH indicator. The left half of the bipolar membrane is positively charged, whereas the right half is negatively charged. Figure taken with permission from Cheng & Guo (2009).

large viscous dissipation rate at that scale. Indeed, we are not interested in charge polarization by pressure-driven flow through charged nanopores, which is responsible for the electroviscous and streaming potential phenomena (Hunter 1981) and was suggested as a mechanical-electrical energy-conversion technique (Heyden et al. 2006). As shown in the next section, the mechanical energy dissipation rate of viscous flow in nanochannels is large compared to the current generated. We hence do not expect the efficiency of such an electricity-generation mechanism to be high. Nor are we interested in the contribution of electro-osmotic flow to ion flux in the nanopores. Again, a simple scaling theory will show that it becomes insignificant with decreasing nanochannel size.

Instead we review recent results showing that ion flux through a nanopore is strongly affected by the flow not within the pore but at the entrance and exit of the pore, where it connects to channels with supermicrometer scales and with much less hydrodynamic resistance. The relevant flow can be driven by an imposed pressure gradient or an applied electric field, or it can result from a natural microscale instability at the entrance. This strong hydrodynamic effect on the ion current is realized when ion transport through the nanopore is controlled by the ion flux at the entrance. Entrance gating of the nanopore ion current occurs often and is in fact a major design consideration for liquid fuel cells—it occurs near the limiting-current condition (Levich 1962). We hence review some recent results for the onset of the limiting current, which involves reviewing the classical membrane theories. Consequently, we show that microvortices at the membrane entrance are in fact responsible for the transition from the limiting-current region to an overlimiting region with much higher current flux. The limiting-current region corresponds to the depletion of ions at one nanopore entrance or one membrane surface and hence can be used to desalt the solution and filter/concentrate charged analyte (Kim et al. 2010).

Other than the practical importance of these effects of hydrodynamics on ion flux through nanopores or nanoporous membranes, the underlying hydrodynamic phenomena are also rich. Although the hydrodynamics occurs outside the nanopore, the dimension of the resulting vortices is still quite small—smaller than 1 mm typically. The relevant hydrodynamics hence involves microscale vortices, vortex instabilities, and even turbulence-like eddy fluctuations with vortex-pairing dynamics that creates a range of vortex sizes, all at miniscule Reynolds numbers! These vortices are driven by charge polarization that results from ion depletion, and both the ion concentration and flow fields are sensitive to the disparate length scales at the nanopore/microreservoir

Limiting current: asymptotically approached value of the ionic current with increased applied voltage, corresponding to the complete depletion of ions at the counterion influx side of the ion-selective membrane

junction. These entrance electrokinetic vortices hence are related to Moffat vortices at geometric singularities (Moffatt 1964), and their dependence on singular electric fields is similar to that seen in direct current (DC) Taylor cones (Taylor 1964) and alternating current (AC) cones (Chetwani et al. 2008)—all phenomena amenable to local self-similar analysis because of their lack of natural length scales. Singularities, instabilities, turbulence, the continuum of length scales, self-similar solutions, and vortex pairing are among the phenomena that are dear to every hydrodynamicist. It is our hope that this review attracts the hydrodynamic community to this new area of microhydrodynamics driven by nanoscale electrokinetics.

Donnan potential:
arises between the interstitial ion-selective membrane/nanochannel space and the external ionic solution because of a jump in ionic strength

DONNAN POTENTIAL AND PSEUDO-EQUILIBRIUM INTRAPORE ION FLUX

We begin with the classical Guoy-Chapman theory for ion-selective membranes and apply it to a nanopore with overlapping double layers. At equilibrium for a symmetric electrolyte with unit valency, the cation and anion concentrations obey Poisson-Boltzmann equilibrium and depend on the local electric potential ϕ by the Boltzmann distribution, $C^{\pm} = C_0 e^{\mp \phi F/RT}$, where C_0 is the bulk concentration outside the nanopore, and the zero potential reference state is designated to be at that concentration. Herein F denotes the Faraday number, R is the universal gas constant, and T is the absolute temperature. Assuming, for simplicity, the ion distribution in a nanoporous membrane or nanopore does not vary along the wall, but only normal to it, one then obtains the distribution of the net charge of mobile ions in the membrane, $-2FC_0 \sinh(\phi F/RT)$. Because the nanopore is overall electroneutral, the surface charge density σ_s must balance this net space charge within the nanopore, and hence the Donnan potential in the interstitial space is $\phi_d = \frac{RT}{F} \sinh^{-1}(\frac{\sigma_s}{FC_0 h})$, where the length scale h is the twice the ratio of the interstitial volume to surface area—the channel height for a straight wide channel, half the channel height for a square channel, and the radius for a cylindrical nanopore. Using the wide channel as a model, one can define an effective volume concentration for the space charge $\Sigma = -\frac{2\sigma_s}{Fh}$ such that $\phi_d = \frac{RT}{F} \sinh^{-1}(-\frac{\Sigma}{2C_0}) = \frac{RT}{F} \ln(-\frac{\Sigma}{2C_0} + \sqrt{(\frac{\Sigma}{2C_0})^2 + 1})$ with the double-valued inversion of the hyperbolic sine. Other than this explicit expression for the Donnan potential, the last expression also allows the determination of the mobile ion concentration in the interstitial space $C^{\pm} = \pm\frac{\Sigma}{2} + \sqrt{(\frac{\Sigma}{2})^2 + C_0^2}$ such that the ionic strength within the space is $C_{slot} = \frac{C^+ + C^-}{2} = \sqrt{(\frac{\Sigma}{2})^2 + C_0^2}$, which is roughly $\frac{|\sigma_s|}{Fh}$ in the ideally selective limit, and the charge density of the mobile ions is $\rho = F\Sigma = -\frac{2\sigma_s}{h}$. For perspective, at the maximum surface charge density of one electron per 10 nm², a 10-nm nanopore will have a local ionic strength of approximately 10 mM. Although this concentration is much higher than the bulk for an ion-selective nanopore with overlapping Debye layers, the pore remains the rate-controlling region for ion flux through the pore. Even at deionized water conditions in the bulk, 10 mM is only four orders of magnitude higher than the bulk concentration. In contrast, a single nanopore is often six orders of magnitude smaller in cross section than the electrodes or microreservoir. Hence, in most cases, the intrapore conductance is ion-flux controlling, and one does not need to be concerned with ion-flux resistance outside the pore.

This simple equilibrium theory allows for order-of-magnitude estimates of several transport coefficients for near-equilibrium fluxes that do not perturb the above equilibrium distributions. These estimates allow us to evaluate several nanofluidic phenomena and technologies that have been suggested in the literature. The electro-osmotic velocity in a nanopore with overlapping double layers scales as $u \sim \frac{\rho h^2 E_{\parallel}}{4\eta} = -\frac{\sigma_s h E_{\parallel}}{2\eta}$, where $E_{\parallel}$ is the tangential field, and η is the dynamic viscosity. In contrast, the electrophoretic velocity of an ion with size a and net charge q is

$u_p = q E_{\parallel}/6\pi\eta a$. Hence the effect of electro-osmotic flow on ion flux becomes negligible when $|\sigma_s| \ll \frac{q}{3\pi ab}$. A rule of thumb for the surface charge density is that its maximum is one electron charge per Bjerum length l_B [which equals $\frac{e^2}{4\pi\varepsilon_0\varepsilon_r\kappa_B T} \sim 5$–10 nm, where $\varepsilon_r \sim 5$–10 is the relative dielectric constant of the substrate (Pyrex/polysilicon)] squared, as even closer packing would mean Coulombic repulsion between a condensed charge, and the next condensing charge would exceed the thermal energy gained. Hence, for monovalent buffers, the electro-osmotic contribution to ion flux is negligible when $\frac{l_B^2}{3\pi ab} \gg 1$. A proton, a common cation, is believed to have a hydrodynamic radius as small as 10^{-4} nm, and larger ions rarely exceed 10^{-2} nm. Hence osmotic convective current flux is important only for nanopores much larger than l_B^2/a or ~ 100 nm in radius. Using the Einstein-Stokes relationship to relate the electrophoretic mobility to the diffusivity of the ion, one can express this criterion as a dimensionless Péclet number $Pe = \frac{|\sigma_s| b RT}{2\eta FD} \ll 1$, where the characteristic length scale $\frac{2\eta FD}{|\sigma_s| RT}$ is approximately 10 nm, with D the diffusion coefficient. Because the Debye length for aqueous solutions never exceeds 100 nm, this phenomenon is not important for electrolytes and would occur only for organic solvents with low ionic strengths, as was measured by Wang et al. (2006).

Conversely, if there is no applied electric field, the current flux due to a pressure-driven flow with a characteristic flow rate of Q scales as $Q\rho$, whereas the mechanical input pumping power scales as $\eta l Q^2/b^4$, where l and b are the length and radius of the nanopore, respectively. As such, the net current per unit power input is $\rho b^4/\eta l Q$, which becomes extremely small for nanopores.

The equilibrium ionic conductance of a nanochannel of length l, height b, and width w for a monovalent symmetric electrolyte can now be estimated from the ion concentrations:

$$I/V = F\mu \left(C^+ + C^-\right)\frac{wb}{l} = 2F\mu\sqrt{\left(\frac{\Sigma}{2}\right)^2 + C_0^2}\,\frac{wb}{l}, \tag{1}$$

where $\mu = FD/RT$ is the ion mobility. Consequently, when the nanopore becomes highly selective, $\Sigma/2 \gg C_0$, the conductance becomes independent of the bulk concentration C_0. Such a curious conductance dependence on bulk ionic strength is shown in the data of Yossifon et al. (2010b) in **Figure 2**, in which the ion selectivity is observed to occur below 1 mM of KCl solution. The double layer begins to overlap below this ionic strength, and the ion selectivity becomes
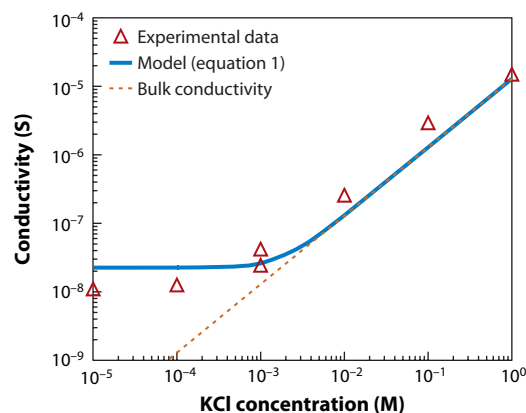
Figure 2

Conductance of an aqueous-filled, polysilicon/Pyrex glass, wide nanoslot (2.5 mm), as a function of the ionic strength C_0. The symbols denote experiment, the continuous line is the model (Equation 1), and the dashed line is the bulk conductivity (Equation 1 with $\Sigma = 0$). Figure taken from Yossifon et al. (2010b).

more pronounced. Even before the double layers overlap, weak ion selectivity can still occur at the transition region near 1 mM. This method of estimating the ion selectivity of a nanochannel has now become standard.

There is considerable evidence that at high voltages, ion depletion and enrichment occur within the pore such that the above equilibrium distributions are no longer valid. Such depletion is most pronounced for conic pores and other pores with asymmetric pore geometries or asymmetric surface charge and is in fact responsible for rectification phenomena in conic pores, as shown in **Figure 1** (Cheng & Guo 2010). However, even with such internal deviation from the equilibrium distribution, the pore remains the ion-flux-controlling region between two electrodes with the lowest conductance. From equilibrium theory, it is clear that a bulk concentration-independent conductance (Equation 1 for the limit of $\Sigma/2 \gg C_0$) can be defined for the nanopore, and hence the *I-V* curve should be linear (constant resistance). It is until ion depletion occurs at the entrance of the nanopore that ion-flux resistance shifts from the intrapore region to the pore entrance and nonlinear *I-V* characteristics begin to develop. The break in the linear *I-V* curve at higher voltages is clearly seen in the data of Yossifon et al. (2009b) in **Figure 3**. A lower differential conductance is observed beyond a critical voltage, with an *I-V* characteristic quite distinct from the hysteretic one in **Figure 1**. This is commonly referred to as the limiting-current region. However, at another, even higher voltage, the differential conductance undergoes a discontinuous jump to another high conductance value at an overlimiting region. It is the overlimiting transition that is controlled by hydrodynamics, but the origin of this hydrodynamic instability can be traced back to the entrance ion-depletion phenomenon that occurs in the limiting-current region.

LIMITING CURRENT, ENTRANCE ION DEPLETION, AND EXTENDED POLARIZATION

For electroneutral ion flux, the Nernst-Planck equation for ion transport in a symmetric electrolyte exhibits a curious mathematical invariance—the opposite electromigration fluxes of the two ions cancel each other when the two ion-transport equations are summed to produce a diffusion equation for $C = \frac{C^+ + C^-}{2}$, with a diffusivity that is twice the symmetric ionic diffusivity. When the symmetric electrolyte is electroneutral, the two ions must exist in equal concentration $C^+ = C^- = C$, and hence the solution of the diffusion equation for C also offers the solution for $C^\pm$, without solving the nonlinear Nernst-Planck equation or the Laplace equation for the potential! Moreover, if the bulk counterions C^+ enter an ideally cation perm-selective nanoslot or nanoporous membrane, such that a zero-flux coion exists everywhere, then the electromigration flux of the counterions is equal to the diffusive flux, $-\frac{DF}{RT}C^+\nabla\phi = -\frac{DF}{RT}C^-\nabla\phi = -D\nabla C^- = -D\nabla C^+$. Hence the total current density consisting of the counterion flux only is twice the diffusive flux $j = -2D\nabla C^+ = -2D\nabla C$. It was Levich (1962) who first realized that an ion-selective membrane will soon deplete the counterions at the membrane surface where counterions enter (and enrich the counterions at its opposite surface). As a result, an ionic concentration gradient is established in the bulk electrolyte until the membrane concentrations of both ions vanish at the membrane surface. For a sufficiently large membrane surface, this limiting-current density is then $j_{\lim} = -2DC_0/L$, where L is the diffusion length typically taken to be the distance from the membrane surface either to the electrode in the case of stagnant diffusion layer or to the edge of a well-mixed region. To obtain the limiting current, Levich simply multiplied the limiting-current density by the total pore area of the membrane.

As seen in **Figure 3a**, this limiting current is also observed for ion-selective nanochannels, and its associated differential conductance value is typically much lower than that predicted by the channel conductance in Equation 1. Hence once ion depletion is completed at the nanochannel
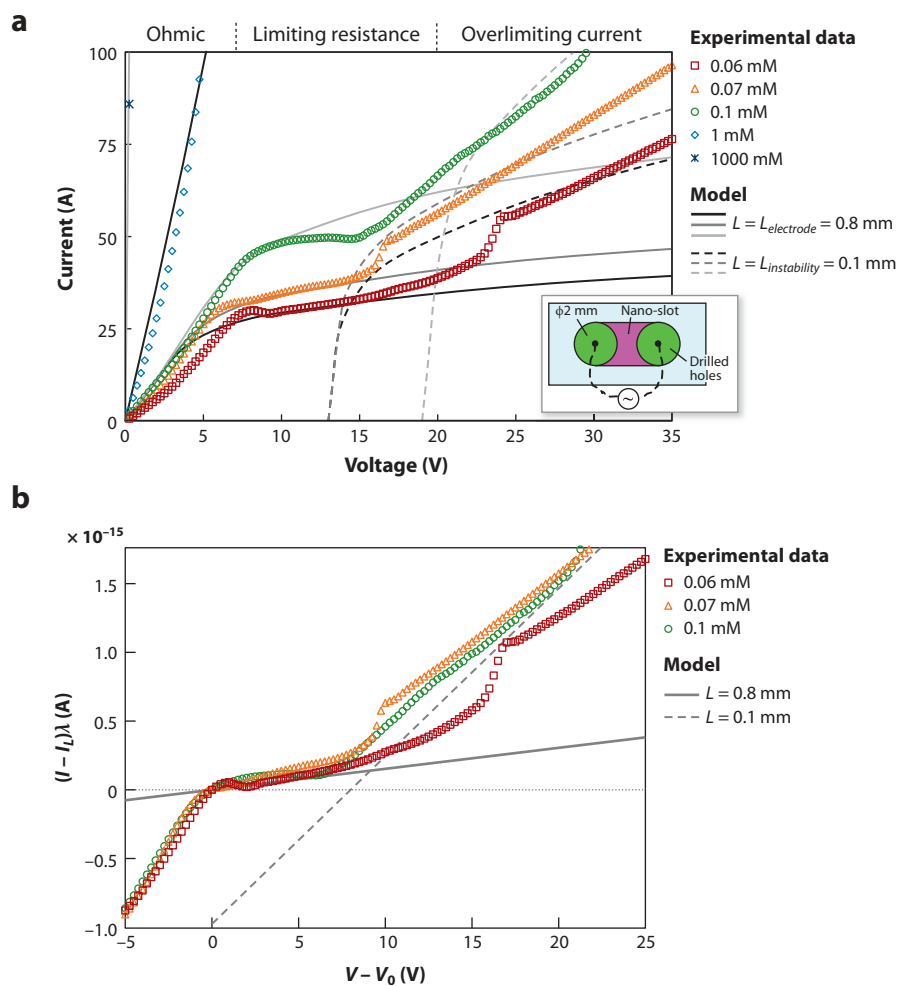
Figure 3

(*a*) Current-voltage characteristics of a nanoslot (*inset*) for varying ionic strengths. The symbols denote experiment, the continuous lines represent the model $L = L_{electrode} = 0.8$ mm, and dashed lines represent the model $L = L_{instability} = 0.1$ mm. (*b*) Collapse of large-current data in panel *a* using Ben & Chang's (2002) theory. The continuous line represents $L = L_{electrode}$, and the dashed line represents $L = L_{instability}$. Figure taken from Yossifon et al. (2009b).

entrance, the highest resistance for ion transport shifts from the intrapore region to the entrance region. Unlike membranes, the nanoslot tends to have a much smaller cross-section area than the adjacent microreservoir or the electrode. In fact, the resulting field-focusing effect is why intrapore ion conductance is less than bulk ion conductance at low voltages, even though the pore has a higher volume conductivity. Fortunately, as only the diffusion equation is at play, only its solution at the entrance geometry is relevant. Depending on the width of the nanoslot relative to its height, the nanochannel resembles a line or a point sink for the ions, with singular fundamental solutions to the diffusion equation that scale as *lnx* or *1/x* relative to the normal coordinate *x*, respectively. Recent confocal images of the fluorescent ion field (Yossifon et al. 2010b) outside the entrance for nanoslots of variable width (but constant height) do indeed exhibit these geometry-dependent
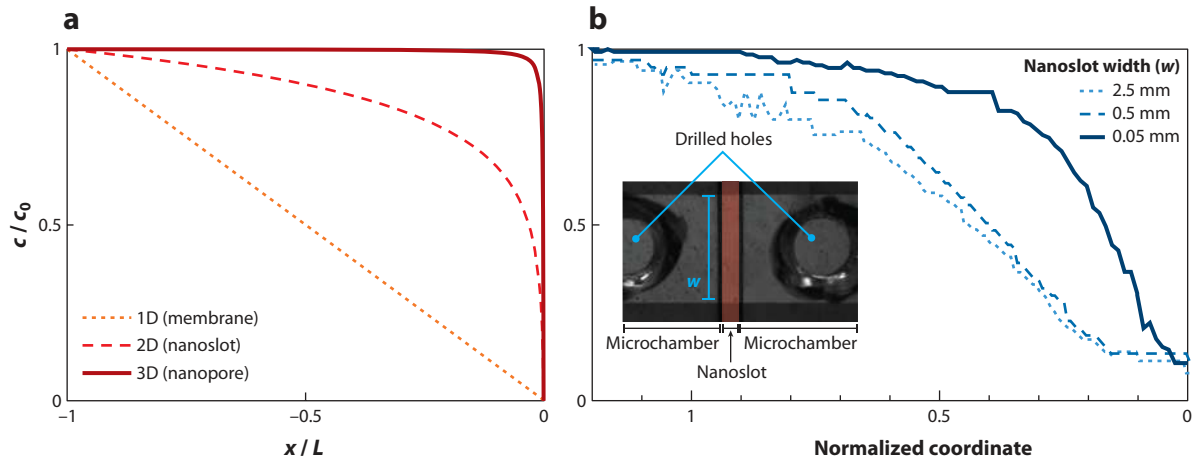
Figure 4

(*a*) Calculated concentration profiles at the anodic side of a pseudo-1D membrane, 2D nanoslot, and 3D nanopore, exhibiting an increasing field-focusing effect. (*b*) Measured concentration profiles at 10 V for the different nanoslot widths, *w*, clearly showing an increase in concentration gradient with decreasing nanoslot widths. (*Inset*) Optical microscope image (top view) of the chip with the widest (2.5-mm) nanoslot (emphasized with a *red background*). Figure taken from Yossifon et al. (2010b).

singular concentration profiles, as seen in the images of **Figure 4** and the imaged concentration profiles. The depletion length is much longer for a wide slot and approaches a constant as the slot width narrows. For a wide nanoslot with *lnx* concentration profile at the entrance, the limiting current has been shown by Yossifon et al. (2009b) to be $I_L = -\frac{\pi F D C_0 w}{\ln(b/L)}\left(\frac{\gamma+1}{\gamma-1}\right)$, where the nonideal perm-selectivity is captured by the parameter $\gamma = C^+(\Sigma)/C^-(\Sigma)$, and L is now the radial length of the depletion region. The critical voltage for the onset of the limiting-current region due to the entrance effect can then be obtained by multiplying this current density by the nanoslot area and relating it to the current due to intrachannel flux in Equation 1:

$$V_0 = -\frac{\pi RT/F}{2(b/l)\ln(b/L)}\left(\sqrt{\left(\frac{\Sigma}{2C_0}\right)^2 + 1}\right)^{-1}\left(\frac{\gamma+1}{\gamma-1}\right). \qquad (2)$$

This estimate for the onset of the limiting current for a wide nanoslot is favorably compared with experimental data in **Figure 3*a***.

Similar expressions for the onset of the entrance effect for nanopores and other geometries can be found in Yossifon et al. (2010b). An important observation is that for isolated small pores, the depletion length L can never exceed the pore radius and hence has a high flux per pore due to the $1/L$ scaling for the diffusive flux of such point sinks. When the pores are separated by a distance less than their radius, their depletion regions overlap. Consequently, a row of nanopores behaves like a line sink or a wide nanoslot, whereas a two-dimensional (2D) array of nanopores behaves like a flat membrane. Thus the ion transport through the nanopore, nanoslot, and membrane can be modeled using spherical, cylindrical, and Cartesian coordinate systems, respectively. Both the line and 2D surfaces exhibit lower flux per pore than isolated nanopores because of the decreased field-focusing effect and consequently its associated increased depletion length L. However, because they have more pores per area, there exists an optimum pore separation for maximum conductance for a given surface area and nanopore radius.
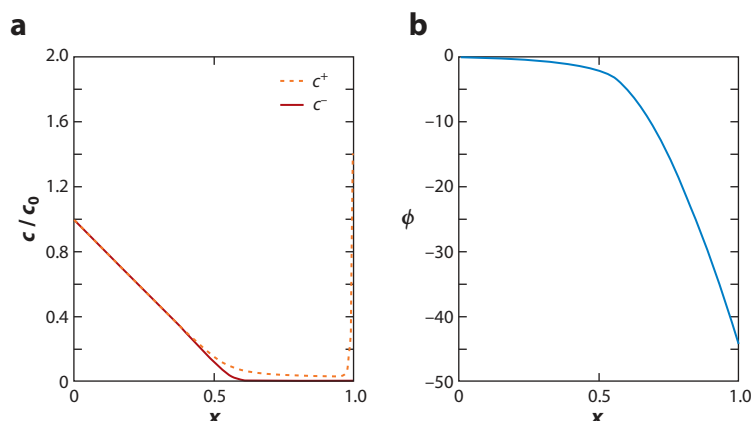
Figure 5

(*a*) Extended polarization at the surface of a membrane situated at $x = 1$ that only allows cation flux. The counterion concentration assumes a flat profile in the inner extended polarization region. Both the cation and anion concentrations approach a linear profile in the outer electroneutral region, but the extrapolated linear profile has a negative intercept—the effective negative surface concentration (surface charge density) that is sustaining the field gradient in the outer region. (*b*) The electric potential blows up logarithmically in the inner extended polarization region. The outer potential has an effective surface value that is related to the effective surface concentration. Figure taken from Ben & Chang (2002).

However, as seen in **Figure 3a**, although the onset voltage for entrance depletion and flux-controlling resistance is accurately captured, the current does not reach a constant asymptote as predicted by Levich's theory. This subtlety of the *I-V* curve results from another singular solution, not for the diffusion equation but for the electric potential. In the limit that both ion concentrations approach zero, the Boltzmann distribution for the zero-flux coion at ideal selectivity would stipulate that the potential must approach negative infinity. We can demonstrate this more explicitly for a pseudo-1D membrane without electric field or concentration focusing. The electroneutral solution to the diffusion equation is then linear in the normal coordinate x, $C^+ = C^- = C = C_0 - \frac{j}{2D}x$ for a given ionic flux j. Consequently, the potential distribution within the electroneutral region has a logarithmic dependence on the normal coordinate $\phi = \frac{RT}{F} \ln(1 - \frac{j}{2DC_0}x)$. At the entrance ($x = 1$), the potential approaches negative infinity in a logarithmic manner when the interfacial concentration C_i vanishes. The solution of the Nernst equation by Ben & Chang (2002), reproduced in **Figure 5**, indeed shows this logarithm blow up the asymptote of the potential near the membrane surface.

This is clearly impossible, and Rubinstein & Shtilman (1979) first postulated that this potential singularity must be smoothed by an extended polarized region that matches the electroneutral fundamental solution of the diffusion equation. Ben & Chang (2002) carried out the matched asymptotics from the electroneutral region with the extended polarized region and obtained the following prediction of the ionic flux beyond V_0:

$$j - j_{\text{lim}} = 3D\varepsilon_0\varepsilon_f \frac{(V - V_0)}{F\lambda L^2}. \tag{3}$$

We offer a rough scaling theory for this correction to Levich's limiting-current theory—as the interfacial concentration C_i vanishes, the current does not approach a constant asymptote, but rather the differential conductance approaches a low constant, much lower than the pore conductance of Equation 1. Away from the logarithmic singularity at the interface, the potential has a linear

profile and extrapolates to the membrane as $\phi \sim -\frac{RT}{F}\frac{j}{2DC_0}x$ as in a well-mixed electroneutral region prior to the establishment of the diffusive linear concentration profile. The outer potential field in the bulk, when extrapolated from the bulk toward the membrane, has a nonzero apparent potential V_0 at the interface that is different from the true membrane potential. The electric field from the membrane is screened by the Debye-layer counterions in the absence of flux, but the depletion effect removes this screening. The extended polarization also contributes to a significant excess potential drop. Both effects produce a field jump across the depletion and extended polarization regions that can be modeled as a negative surface electric field (positive potential gradient) on the membrane, which can be related to an effective negative surface charge density on the membrane $\varepsilon_0\varepsilon_f(V-V_0)/L$. To assure continuity of the concentration field, there must be a corresponding effective interfacial concentration, when the bulk concentration profile is extrapolated from the bulk, that is negative. The effective negative surface charge density can be related to the negative effective interfacial concentration by dividing the former by the Debye length λ, the length scale of the inner extended polarized region, to produce $C_i \sim -\frac{3\varepsilon_0\varepsilon_f(V-V_0')}{2F\lambda L}$, which is evident in **Figure 5**. Because $j = 2D\frac{C_0-C_i}{L}$, the effect of extended polarization on the current in Equation 3 is then captured once one imposes the condition that the $C_i = 0$ limit corresponds to Levich's limiting current.

As seen in **Figure 3b**, despite this near-onset limitation, scaling Equation 3 collapses the nanoslot *I-V* data of Yossifon et al. (2009b) in the limiting-current region, with $L = 0.8$ mm corresponding to the actual microreservoir dimension. Most surprisingly, the overlimiting data also collapse and can also be captured by Equation 3 if L is reduced from 0.8 mm to 100 μm. There is hence a new mechanism that has reduced the depletion length by a factor of eight, leading to the larger current in the overlimiting region. Hydrodynamics is responsible for choosing this new depletion/diffusion length scale.

MICROVORTICES GENERATED BY EXTENDED POLARIZATION

Extended polarization exists on one membrane surface or one nanopore entrance over a length scale comparable with the Debye length and larger. Unlike polarization due to surface charge in an equilibrium Debye layer, the extended polarization results from an external field and can be sustained only if there is a flux of ions into the membrane or nanopore—it is a nonequilibrium phenomenon. This extended polarization can also drive tangential electro-osmotic flow if a tangential electric field exists. In fact, this is the basis of Dukhin's (1991) electro-osmotic flow of the second kind for surfaces with curvature. Because of the curvature, the normal field that drives normal ion flux into the granule changes along the surface. From Equation 3, the flux-induced potential at the surface V_0 is proportional to the normal flux, which is proportional to the bulk normal electric field. Hence the local velocity scales as the product of the normal and tangential field components. This implies that, for a conducting ion-selective granule, the induced electro-osmotic velocity is maximum not at the equator (zero normal field) or pole (zero tangential field), but at an intermediate azimuthal position close to 45°. This variation in the induced tangential electro-osmotic velocity along a curved surface necessarily implies the formation of vortices, as flow continuity stipulates that the tangential pressure gradient must exist to drive a vortex—the tangential flow to the equator is forced back further away from the surface in a vortex pair around the spherical granule. Because only the influx side of the granule can sustain such extended polarization, a vortex pair exists only on the side of the granule when the net ion current enters the granule. This is the basis of Dukhin's electro-osmosis of the second kind and superelectrophoresis for ion-exchange granules—because of the asymmetry of the vortex pair, there is a net electrophoretic motion due to this flux-induced electro-osmosis on a granule (Barany et al. 1998). Not surprisingly, the

superelectrophoretic velocity scales quadratically with respect to the applied field with an effective zeta potential of *Ea*, where *a* is the granule radius (Dukhin 1991). At high Péclet numbers, however, convection may alter the ion flux and hence perturb the scaling of Equation 3 and the field scaling of the superelectrophoretic velocity of ion-selective granules (Ben et al. 2004).

It is less obvious that the extended polarization layer is unstable on a flat membrane and hence can sustain a microvortex instability. This theory was first advanced by Rubinstein & Zaltzman (2000). They argued that the concentration and potential fields of the extended polarization inner region, as shown in **Figure 5**, create a thin film near the membrane, much like a free surface. When the polarization layer thins because of some kind of localized disturbance, the nearly singular electric field of **Figure 5** becomes even more intense, thus creating a high–Maxwell pressure εE^2 spot at the membrane surface. This high-pressure spot drives liquid radially away from it on the membrane surface and, again because of flow continuity, produces a vortex pair on a linear membrane (a wide nanoslot) and a vortex torus on a planar membrane, both with a diverging stagnation point on the membrane. This diverging stagnation flow pushes the extended polarization at the stagnation point, thus providing a linear positive-feedback mechanism. This mechanism is quite similar to other classical free-surface hydrodynamic instabilities such as the free-surface Rayleigh-Bénard instability with a high normal temperature gradient in a film. Here the temperature gradient is replaced by a potential gradient (field) and the hydrostatic pressure dependence on temperature by the Maxwell pressure gradient dependence on the field. If the disturbance is not localized, vortex streets and vortex arrays are hence expected. Similar to other hydrodynamic instabilities, we expect this positive feedback mechanism to be stabilized by viscosity at short length scales and be saturated by nonlinearity at large length scales. Hence one expects a particular vortex size to be selected, and this vortex size corresponds to the depletion length *L* of the overlimiting region in **Figure 3*b***.

Earlier experiments (Maletzki et al. 1992, Rubinstein et al. 2002) provide some support of this theory. The overlimiting region is not observed if the electrolyte is replaced by a hydrogel. Near the onset, the fluctuation of the overlimiting current does exhibit certain fundamental frequencies, corresponding perhaps to flux fluctuations produced by vortices of a given size. However, the fluctuation becomes broadbanded further from criticality as in the classical transition to turbulence.

Yet this vortex instability and its connection to the overlimiting current have been verified experimentally only in the past two years (Rubinstein et al. 2008, Yossifon & Chang 2008). Realizing that a nanoslot is a good model for a linear membrane in a planar system, Yossifon & Chang (2008) used confocal imaging of fluorescent charged dye to detect these vortices. The extended polarization may be less than 1 μm thick and is hence not detectable, but the microvortices sustained by it are 10 to 100 times larger. Nevertheless, as the mixing action of the vortices can quickly disperse the dye concentration within the vortex, imaging the steady or stationary vortices is difficult. The evolution dynamics of the vortices, presumably involving the merging of small vortices, that is responsible for the turbulent broadband fluctuation observed (Maletzki et al. 1992) would be almost impossible. Instead, Yossifon & Chang (2008) used a low-frequency (<1 Hz) AC field to entrain the vortices. The depletion region is regenerated at every half-cycle, thus allowing the vortex instability to develop every cycle. The vortex images are shown in **Figure 6**. Larger vortices are observed for longer periods *T*, suggesting that the larger vortices result from merging of the smaller ones at the onset and that the merging is sequential, from one generation of vortices to the next. Some pair-wise coalescence is indeed observed over one half-cycle for larger vortices at large *T*.

The periodic forcing also allows the estimate of the depletion length as a function of the period *T*. As the ionic strength $C = \frac{C^+ + C^-}{2}$ obeys the diffusion equation, the depletion layer is created with a diffusion front that advances away from the membrane. As the front position should scale
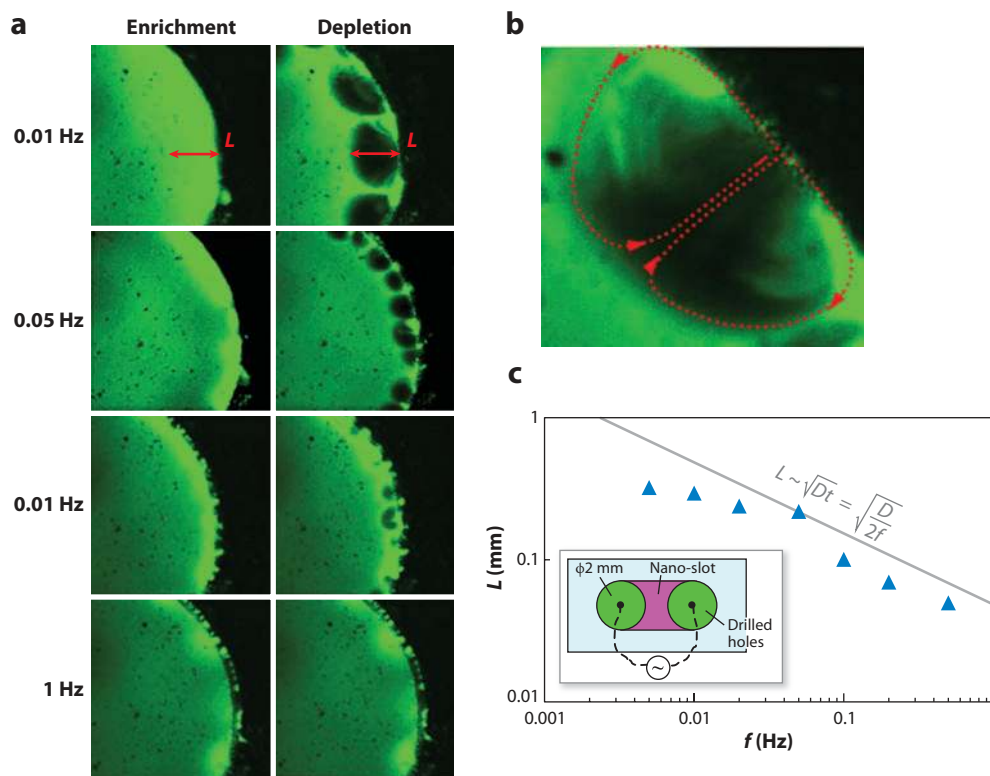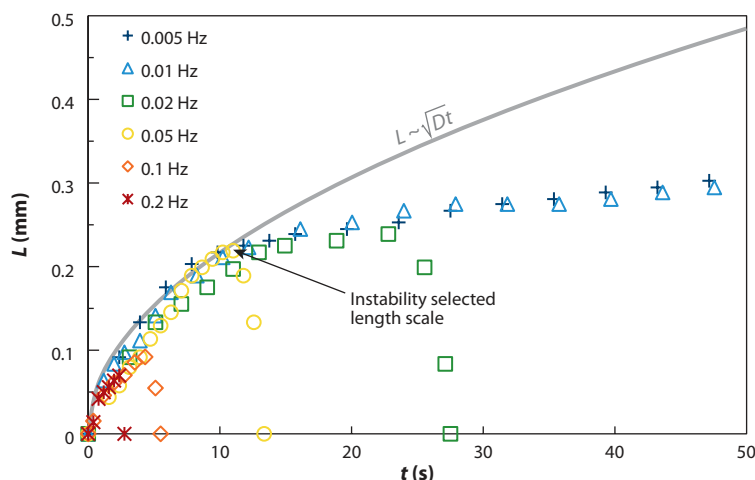
Figure 6

(*a*) Confocal image snapshots of the maximum extent *L* of the concentration polarization layer either in its enrichment (cathodic polarity) or its depletion (anodic polarity) phase at different AC frequencies at the same voltage difference of 80 V peak to peak (see **Supplemental Video 1**; follow the **Supplemental Material link** from the Annual Reviews home page at **http://www.annualreviews.org**). (*b*) A close-up of one of the depletion regions showing its inner structure consisting of a vortex pair. (*c*) A log-log graph of the experimentally measured *L* (*triangles*) versus the frequency and also of a $\sqrt{Dt}$ trend (*continuous line*). (*Inset*) The schematic configuration of the nanoslot device. Figure taken from Yossifon & Chang (2008).

as $\sqrt{Dt}$, the onset of a vortex instability should be signified by a departure from this self-similar scaling. In fact, we expect that the front position should saturate at a constant value, the selected depletion length, once it departs from the self-similar scaling. This is indeed observed in the measured depletion-layer thickness as a function of time at different periods in **Figure 7**. For smaller periods, the observed vortices are not fully established and hence cannot suppress the diffusion-layer growth, and the depletion front obeys the self-similar scaling. Beyond a critical period, corresponding to the onset time of the fully established vortices, the front position breaks away from the self-similar dynamics and saturates at a constant asymptote within the depletion half-cycle. In fact, when a similar nanoslot is used, the selected depletion length is exactly 100 µm, the depletion length used to collapse the overlimiting *I-V* data of **Figure 3b**. Pair-wise merging of the vortices evolves until a particular vortex size and depletion length are reached. These values are observed to be a function of the width and height of the microchannel outside the nanoslot, as viscous dissipation seems to be responsible for the arrest of the vortex-pairing dynamics. The vortex instability hence selects the depletion length.

Depletion front:
the self-similar propagating electroneutral diffusion front that propagates from the ion-depleted region at the nanoslot entrance toward the bulk region
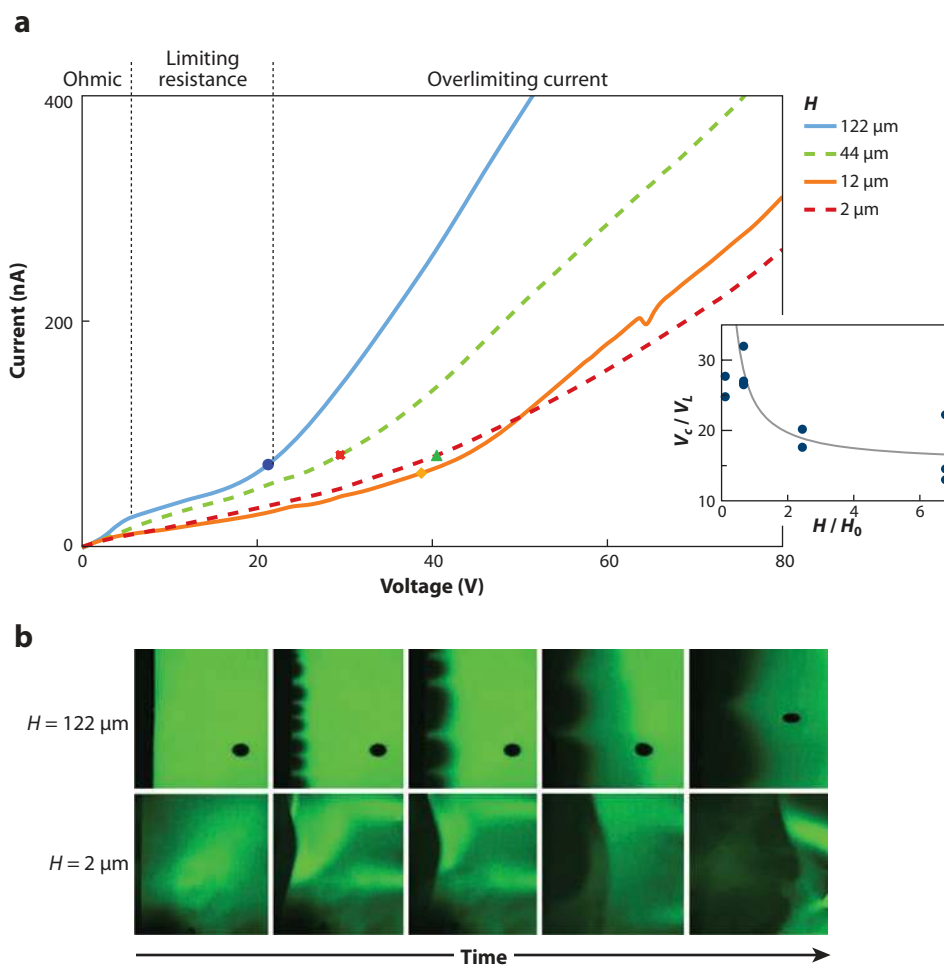
Figure 7

Time evolution of the instantaneous depletion-front thickness for different frequencies at the same voltage difference of 80 V peak to peak. Also depicted is the $\sqrt{Dt}$ scaling (*continuous line*). A clear break from the self-similar scaling is observed at $L \sim 220$ μm. Figure taken from Yossifon & Chang (2008).

That the microchannel height determines the final selected vortex size and depletion length was more conclusively verified by Yossifon et al. (2010a) using a wide nanoslot (of fixed height) connecting symmetric microchambers of varying height on its two opposite sides. The selected depletion-layer length, vortex size, overlimiting current, and even the onset voltage for the over-limiting behavior are shown to be sensitively dependent on the connecting microchamber height (see **Figure 8**). The vortex-pairing dynamics that occurs for tall microchambers is observed to proceed until only two vortex pairs survive. In contrast, vortex formation is not observed for short microchambers. The final depletion length is also quite distinct for the two cases, with a much longer depletion length for the shorter microchamber without the vortex instability. In fact, the depletion length extends to the electrode in the vortex-free case. It is expected that intermediate depletion lengths could be chosen with different numbers of final vortices for intermediate microchamber heights. Simple scaling arguments relating the microchamber depth to the effective fluid viscosity [$\eta_{eff} \sim 12\eta(w/H)^2$, where H is the microchamber height and w is the nanoslot width] produce experimentally verified scaling dependencies. In the case of a sufficiently deep microchamber, it is the vortex instability electroconvection that counteracts the diffusive growth of the concentration polarization layer. For shallow microchambers, the vortex instability is suppressed, and the diffusive layer grows indefinitely to reach the microchamber end (**Figure 8b**). Recently, the conditions for the propagation of such a shock-like concentration depletion front in a shallow and wide microchannel-nanochannel system were studied theoretically by Mani et al. (2009) and verified experimentally by Zangle et al. (2009). Also, Jung et al. (2009) have recently shown a rectification effect in the overlimiting region across a nanopore connecting asymmetric chambers. It is the different confinement constraints on the electroconvection flow within the microchambers that affected the current. However, with their design (of significant field-focusing), Dukhin's electro-osmosis of the second kind rather than Rubinstein's vortex instability mechanism clearly prevails.

A more smooth transition from the mechanism of Rubinstein's electroconvection instability to Dukhin's electro-osmosis of the second kind for vortex generation was recently shown by Yossifon et al. (2010b). Nanoslots with varying widths were fabricated on a chip (**Figure 4b**, inset) as a simple

a

b

Figure 8

(*a*) Current-voltage curves for 10-μM KCl (strong Debye-layer overlap) buffer concentrations for various microchamber depths. (*Inset*) Measured critical voltage for the limiting to overlimiting transition for varying microchamber depths (corresponding to the symbols in panel *a*). The continuous line represents scaling theory. (*b*) Sequence showing the depletion-layer pattern evolution as a response to a step input of 40 V (see **Supplemental Videos 2** and **3**). In particular, in the case of the deep (122-μm) microchamber, one clearly sees the complex process of wavelength selection by small vortices breaking up through fusion and the transformation into still larger vortices until a quasi-steady-like pattern is formed. In contrast, these patterns do not occur for the shallow (2-μm) microchamber. Instead, a relatively flat concentration polarization layer front is observed to propagate until it reaches the electrode. Figure taken from Yossifon et al. (2010a).

model for capturing the increased field-focusing effect for the transition from a line (wide nanoslot) to a point (narrow nanoslot) sink. Although not a nanoslot array, this decrease of the nanoslot width resembles the increase of channel spacing leading eventually to isolated nanoslots. One of the consequences of the isolation is a single localized depletion region in the narrow nanoslot case (**Figure 9b**) instead of an array of them in the wide nanoslot case (**Figure 9a**) due to Rubinstein's vortex instability. This isolated space-charge region at the pore entrance produces an ejecting vortex pair for isolated narrow nanochannels (**Figure 9c**) or a vortex toroid for isolated nanopores. An
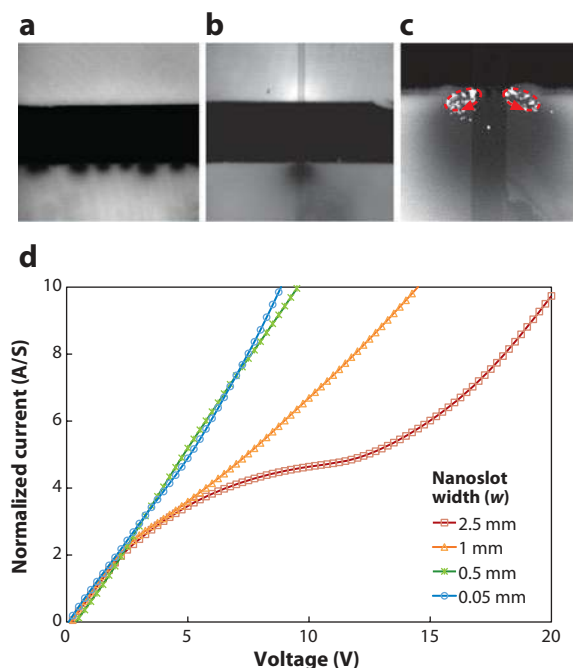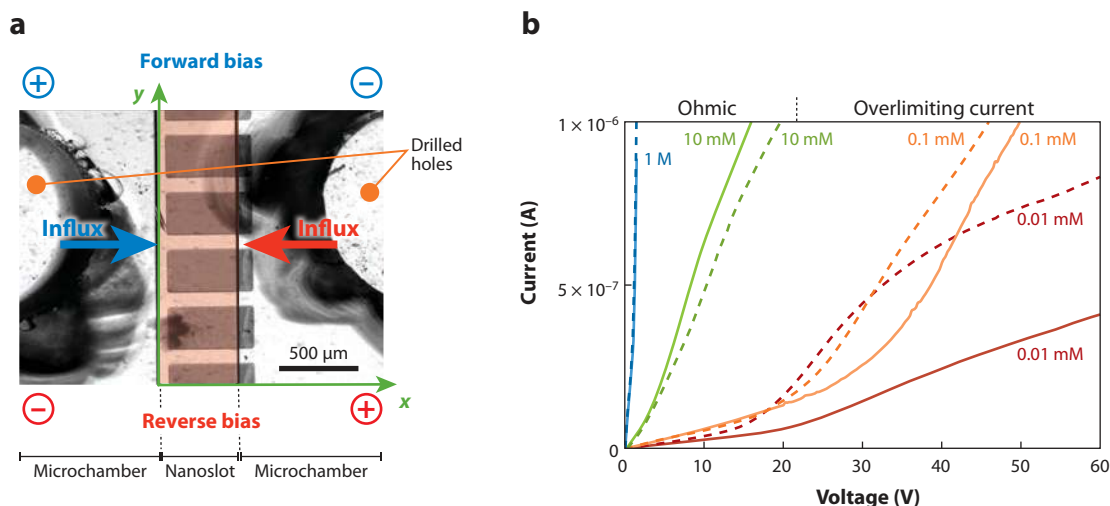
Figure 9

Confocal image snapshots of (*a*) the depletion array pattern for the wide (2.5-mm) nanoslot (see **Supplemental Video 4**), (*b*) a single depletion region for the narrow (50-μm) nanoslot (see **Supplemental Video 5**), and (*c*) a close-up of the narrow nanoslot's depletion region and its associated single vortex pair that ejects from the corners, as observed using fluorescently tagged nanobeads. (*d*) Normalized (by the corresponding Ohmic conductivity) *I-V* data of nanoslots with varying widths, *w*, at 10^{-5}M KCl concentration clearly showing the vanishing of the limiting-resistance voltage window with increased field-focusing effect. Figure taken from Yossifon et al. (2010b).

important consequence is the vanishing of the limiting-resistance window in the narrow nanoslot in contrast to a clear region in the wide nanoslot case (**Figure 9***d*), thus producing very high current density for all voltages that are not limited by Levich's diffusion-limited current. It is directly attributed to the gradual change in field-focusing effects and the appearance of an ejecting vortex pair at the corners, which has replaced the vortex array due to Rubinstein's instability, to dictate the *I-V* characteristics. As corner vortices are not observed for communicating nanoslot arrays, it is expected that pore isolation is necessary for their appearance. The same phenomenon is expected for real membranes with separated pores. As such, the *I-V* characteristics of isolated pores can be dramatically different from communicating ones. This pore communication effect is most likely related to another well-known empirical fact. It is known that nonuniformity of the membrane surface can reduce the voltage range of the undesirable limiting-resistance window (Blaster et al. 2007).

Yossifon et al. (2009a) recently showed that interchannel communication can dramatically affect the electroconvection processes taking place at the microchannel connecting a nanochannel array. A nanochannel array with homogenous surface charge and height (i.e., uniform electrochemical potential) but with asymmetric channel spacing at its opposite entrances (**Figure 10***a*) has been shown to exhibit a strong rectification factor (i.e., ratio of the ionic currents under reverse and forward voltage bias) as high as three (**Figure 10***b*), reminiscent of a semiconductor bipolar diode. As observed, this rectification phenomenon is appreciable only in the overlimiting region, as the extent

Figure 10

(*a*) Asymmetric nanoslot entrances to the microchambers (see **Supplemental Videos 6** and **7**). On the right side, the separate nanoslots exit directly into the microchamber, whereas on the left side they first merge into a wide slot that in turn exits into the microchamber. The influx direction associated with the different voltage biases represents the flow direction of the counterions into the nanoslot (top view). (*b*) *I-V* measurements for varying ionic strengths and applied voltages. The continuous lines represent reverse bias, and the dashed lines represent forward bias. Figure taken from Yossifon et al. (2009a).

of both the vortex-pairing dynamics and the selected depletion length is sensitive to the entrance polarization effects (i.e., space charge) occurring at the nanochannel array's asymmetric opposite entrances. There is no rectification at lower voltages, at which hydrodynamics effects are absent.

Previous low-voltage Ohmic studies of ionic current rectification within nanopores/channels (Cheng & Guo 2007, Karnik et al. 2007, Vlassiouk & Siwy 2007) have attributed this phenomenon to intrinsic nonuniformity of the electrochemical potential along the nanochannel (e.g., by changing the nanochannel cross-section geometry and hence the Debye layer overlap and surface charge patterning). In contrast, the high-voltage rectification of the nanochannel array is because of the combined asymmetry of space-charge polarization and that of the nano-/microchannel geometry at its opposite entrances, resulting in quite different electroconvection behavior. With a clever combination of intrapore and external asymmetries, it is quite possible to design a nanofluidic diode that inverts the rectification direction at a critical voltage—ion current is permissible in different directions at low and high voltages.

SELF-SIMILAR DEPLETION FRONT DYNAMICS AND SELECTION OF EQUILIBRIUM DEPLETION LENGTH

The self-similar evolution of the depletion front and the resulting vortex-merging dynamics have recently been verified by the simulation work of Demekhin et al. (2008) and Kalaidin et al. (2010). In addition to the self-similar diffusion dynamics in the electroneutral outer region, Kalaidin et al. obtained a self-similar structure also for the polarized region. They demonstrated that with the following self-similar transform of the normal coordinate y from the membrane $\eta = y/\sqrt{4Dt}$ and $\varepsilon = \lambda/\sqrt{4Dt}$, the transient 1D Nernst-Planck equation and the Poisson equation reduce to a set

NANOFLUIDIC DIODES

Nanofluidic diodes that exhibit rectification of ion currents have been intensively researched, as they mimic voltage-gated ion channels on cell membranes. The standard assumption is that such PN diodes can be achieved only with asymmetric surface charge in the nanochannel or with converging geometry. The microvortex instability discussed in this review offers another asymmetry that can be manipulated with macroscopic designs outside the nanochannel, or at its very entrance where polarization effects dominate, to produce rectification and possibly other nonlinear ion-flux dynamics—it is a hydrodynamic nanofluidic diode.

of equations with only dependence on η,

$$
\begin{aligned}
2\eta \frac{dC^+}{d\eta} + \frac{d}{d\eta}\left(C^+ \frac{d\Phi}{d\eta}\right) + \frac{d^2C^+}{d\eta^2} &= 0, \\
2\eta \frac{dC^-}{d\eta} - \frac{d}{d\eta}\left(C^- \frac{d\Phi}{d\eta}\right) + \frac{d^2C^-}{d\eta^2} &= 0, \\
\varepsilon^2 \frac{d^2\Phi}{d\eta^2} &= C^- - C^+,
\end{aligned}
\tag{4}
$$

with boundary conditions

$$
C^- \frac{d\Phi}{d\eta} - \frac{dC^-}{d\eta} = 0, \quad C^+ = p, \quad \Phi = 0 \quad \text{at} \quad \eta = 0,
$$

$$
C^+ = C^- = 1, \quad \lim_{\eta \to \infty}\left(\Phi - \frac{J\eta}{2}\right) = \Delta F \quad \text{at} \quad \eta \to \infty,
$$

where J is the dimensionless current at the membrane:

$$
J = C^+ \frac{d\Phi}{d\eta} + \frac{dC^+}{d\eta} \quad \text{at} \quad \eta = 0.
$$

As is in the steady case studied by Ben & Chang (2002), the self-similar solution is insensitive to p. We note that ΔF is the potential drop across the extended polarized region as the Ohmic drop in the electroneutral region has been subtracted from the overall applied voltage in the boundary condition at infinity. Consequently, for a given J, Equation 4 can be integrated to calculate the potential drop ΔF due to extended polarization or vice versa. In **Figure 11**, this self-similar solution is satisfactorily compared to the integration of the full set of transient equations by using the following parameterization, $J(t) = 2j(t)\sqrt{t}$ and $\Delta F(t) = \Delta V - j(t)/2 = \Delta V - J(t)/4\sqrt{t}$, such that for every applied voltage ΔV, the current J can be determined as a function of time t. It is quite clear that the measured current obeys the self-similar evolution dynamics with respect to the (excess) potential drop in the extended polarized region, $\Delta F(t) \sim \Delta V - J(t)/4\sqrt{t}$ for a range of ΔV. This self-similar dynamics provides the same $\sqrt{t}$ diffusive dynamics in the electroneutral region, which was predicted and experimentally verified by Yossifon & Chang (2008) in **Figure 7**. Kalaidin et al. have shown that the self-similar structure extends into the polarized layer, thus mathematically proving the validity of the self-similar solution for the entire domain and even when the extended polarization region is very thick. Indeed, numerical simulation of the full equation on the depletion-region evolution dynamics by Kalaidin et al. is in good agreement with the experimental data of Yossifon & Chang, as seen in **Figure 12**.

Although Kalaidin et al. allowed for an infinitely deep microchannel in their 2D model, such that viscous dissipation is dominated by the sidewalls, they nevertheless observed a selected depletion length in their simulations. How a specific length scale is selected is evident in **Figure 13**. Pairwise

a

b
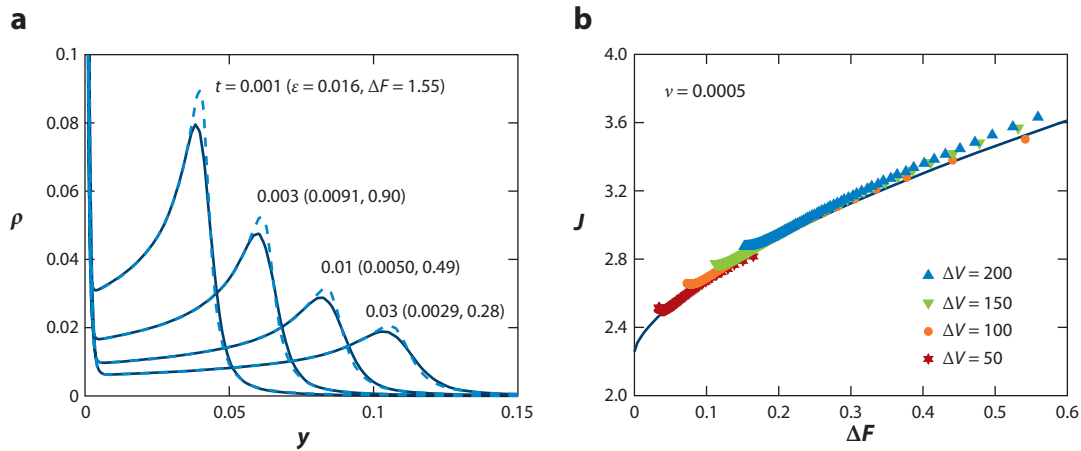
Figure 11

(*a*) Numerically computed evolution of the extended polarized region (*solid lines*) compared with the self-similar solution (*dashed lines*). (*b*) The current during the evolution is found to obey a self-similar relationship with respect to the voltage drop in the extended polarized region for a range of applied voltages (numerical solution, *symbols*; self-similar solution, *solid line*). Figure taken from Kalaidin et al. (2010).

Vortex coalescence:
evolution dynamics of the vortices, presumably involving merging of small vortices, responsible for the turbulent broadband fluctuation observed

vortex coalescence occurs until a critical separation when new vortices nucleate in the quiescent region between two distant vortex pairs—each spike in the charge density generates a vortex pair with a diverging stagnation point at the membrane surface, as is consistent with the images of **Figure 8** for tall microchambers. The turbulence that is observed corresponds to the repeated merging and nucleation of the vortex pairs to select a time-averaged vortex size and a depletion length that are constant. Unlike bulk turbulence, a continuum of vortex size does not appear at every instant in time, and the coarsening does not proceed indefinitely to infinite length scales. Instead, one length scale is selected at a given time until an equilibrium one is selected because of
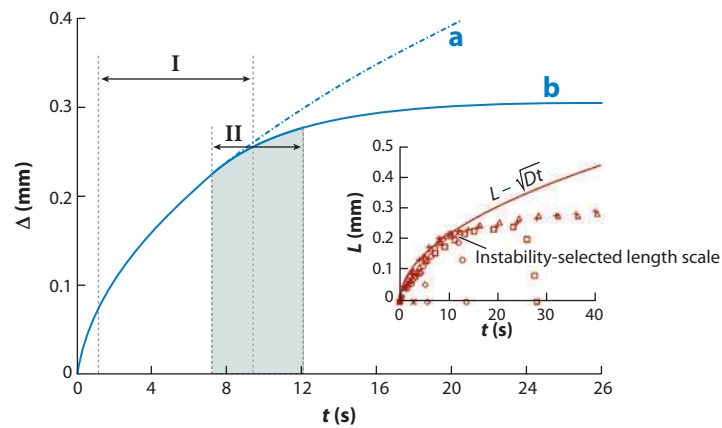
Figure 12

The depletion length from self-similar solution (*a*) and from 2D simulation (*b*) with Yossifon & Chang's (2008) experimental data in **Figure 7** in the inset. Figure taken from Kalaidin et al. (2010). Vortices are not observed in region I and begin to appear in region II. The evolution of these vortices in region II is shown in **Figure 13**.
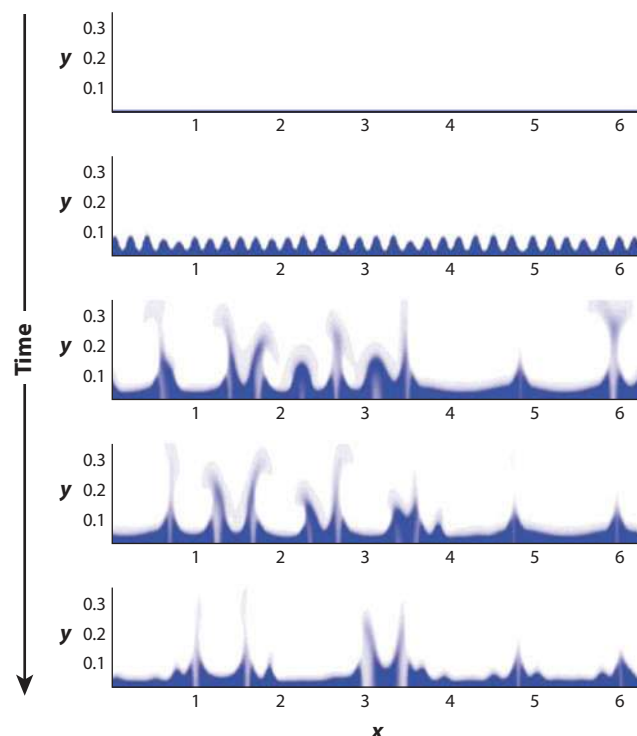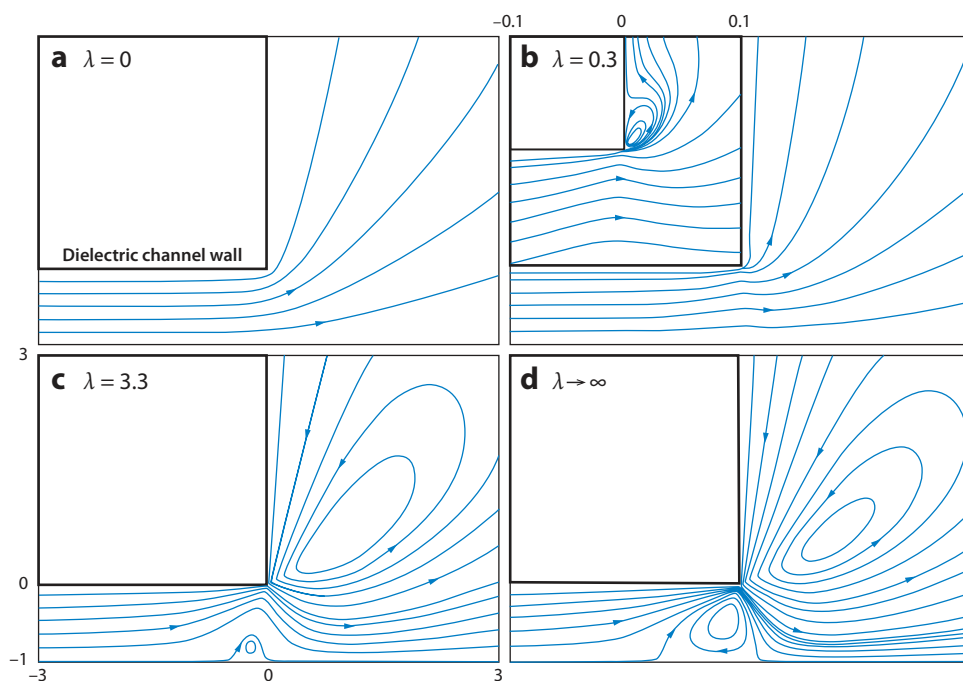
Figure 13

Evolution of the charge density in two dimensions (coordinates are normalized by the space between two electric membranes), showing vortex merging until an equilibrium vortex separation/size when nucleation of new smaller vortices at the quiescent regions balances the loss of vortices by coalescence.

the annihilation and creation dynamics of localized coherent structures—the charge density spikes and vortex pairs. This coherent structure dynamics is quite similar to solitary wave dynamics on falling films; the solitary waves also annihilate each other until new ones can nucleate from the flat film in between to select an equilibrium wave texture (Chang 1994, Chang & Demekhin 2002).

OTHER MICROVORTICES IN ELECTROKINETICS

The vortex instability at the extended polarization layer is the most dramatic vortex-formation mechanism in electrokinetics—and is most important in terms of controlling the *I-V* curve of the nanopore, nanoslot, or nanoporous membrane. However, there are other vortex-formation-dynamics phenomena in electrokinetics. Thamida & Chang (2002) showed that at the sharp inside corners of a turn in a microfluidic channel, there can be significant field penetration across the corner, even if the wall permittivity is low but not zero. Yossifon et al. (2006) derived an effective boundary condition for this field-induced corner polarization and were able to solve the 2D flow problem in a bent channel by conformal mapping. The vortex topologies shown in **Figure 14** are functions of channel geometry, natural zeta potential, and the permittivity ratio. For narrow nanoslots whose small width suppresses vortex instability, such corner vortices can also be observed at the nanoslot entrance, as seen in **Figure 9**. The circulation and symmetry of these corner vortex pairs are quite different from those resulting from the vortex instability at the polarization layer. Nevertheless, they can affect the depletion length of narrower slots.
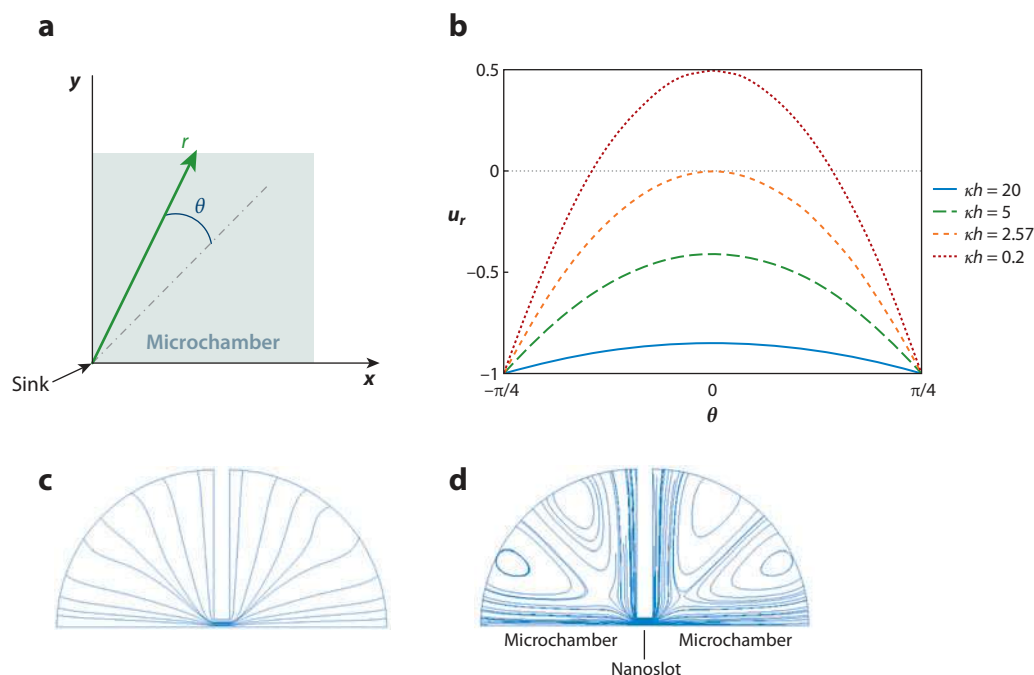
Figure 14

Calculated streamline patterns for a channel width ratio of 10 and varying ratio λ, characterizing the relative importance of the induced and linear respective parts of the zeta potential. Figure taken from Yossifon et al. (2006).

If the microchannel walls outside the nanoslot have surface charges, another mechanism for vortex formation arises: flow balance. A classical electrokinetic theory by Morrison (1970) states that, in the electroneutral region outside the thin Debye layers, the streamlines are identical to the field lines for electrically insulated and flow/ion-impenetrable channels with uniform surface charge. Hence the resulting electro-osmotic flow is irrotational, and there is no internal pressure buildup. This is in fact why electro-osmotic flow cannot push bubbles in a microchannel (Takhistov et al. 2002). If the surrounding film is thick enough, then the field (current balance) through the wetting film also implies liquid-flow balance around a stationary bubble, and pressure cannot build up behind the bubble to push it forward. This theory is why the vortices discussed in this review are so unique. The vortices discussed above revoke this "similaritude" because of ion flux into the membrane (microvortex instability) and field penetration into the wall at corners (**Figure 14**). The hydrodynamic shear of the flow resides entirely within the Debye double layer at the wall, and the electro-osmotic flow in the electroneutral region is a potential flow.

This similaritude breaks down, however, when the electro-osmotic flow is required to pass through a nanoslot or toward a dead end. As the Debye layers overlap across the nanoslot, a net charge $\Sigma = -\frac{2\sigma_s}{Fb}$ exists within it, and in the presence of a longitudinal electric field, the electric body force in the liquid must be balanced by viscous effects. As such, the flow field in a nanopore is not irrotational—a flat velocity profile does not occur for straight channel flow. The Morrison similaritude assumption is hence revoked. In fact, the small or zero flow rate through the nanopore becomes controlling, and pressure must build up at the entrance to eject the excessive incoming electro-osmotic flow. As in Moffat's pressure-driven vortices toward a

a

b

c

d

Microchamber   Microchamber
            Nanoslot

Figure 15

(*a*) Schematics of the 90° wedge and sink simplifications of the micro- and nanochannel junction geometries, respectively. (*b*) Analytically calculated radial velocity versus θ for varying κh values. (*c,d*) Numerically calculated velocity streamline for the case of (*c*) strong and (*d*) weak electrolytes for a model geometry. Figure taken from Yossifon & Chang (2010).

dead-end corner, this imbalance in electro-osmotic flow produces vortices outside the nanopore. The flow problem for the micro- and nanochannel junction could be simplified as a converging sink flow in a 90° wedge (**Figure 15**). In the microreservoir, the thin-Debye-layer assumption holds. Hence the electrostatic problem is obtained by solving the Laplace equation together with Neumann boundary conditions on the microchannel walls ($x = 0, y = 0$) and a sink of strength $m = 2E_0h/\pi$ located at the origin ($x = y = 0$). The Stokes equation can then be solved with boundary conditions (Helmholtz-Smoluchowski slip velocity at the wedge walls), and matching the flow rate with that at the nanoslot (Yossifon & Chang 2010),

$$Q_{nanoslot} = \frac{\zeta^{eq}\varepsilon_0\varepsilon_f}{\mu} E_0h \left(1 - \frac{\tanh(\kappa h/2)}{\kappa h/2}\right), \tag{5}$$

wherein ε_0 is the dielectric permittivity of vacuum, ε_f is the dielectric constant of the fluid, μ is the fluid viscosity, and E_0 is the uniform externally applied electric field within the channel. The Stokes equation admits the separation-of-variables solutions. This solution contains a pressure-driven flow counter to the electro-osmotic flow because of the back pressure that builds up to ensure flow balance into the nanoslot. The resulting radial velocity component ($u_\theta = 0$ due to azimuthal symmetry) is

$$u_r = \frac{1}{\pi r}\left[2 + 3\frac{\tanh(\kappa h/2)}{\kappa h/2}\left(\left(\frac{4}{\pi}\right)^2\theta^2 - 1\right)\right]Q^0_{nanoslot}, \tag{6}$$

where $Q^0_{nanoslot} = (\zeta^{eq}\varepsilon_0\varepsilon_f/\mu)E_0h$ is the electro-osmotic nanoslot flux in the limit of infinitesimally thin Debye layer. The vortices appear at a critical λ/h ratio—where the minimum radial velocity
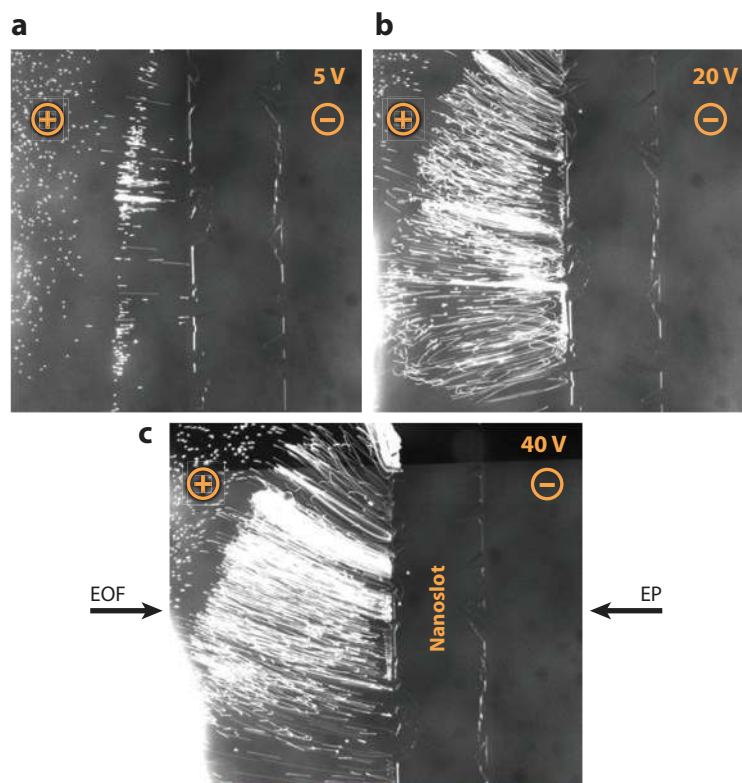
Figure 16

Colloid dynamics for different applied voltages that are (*a*) below 5 V, (*b*) beyond 20 V at the first voltage, and (*c*) beyond 40 V for the second critical voltage (see **Supplemental Video 8**). The dynamics in panel *a* exhibits linear colloid translations within the colloid band, whereas those in panels *b* and *c* exhibit complex toroidal movements. Furthermore, the tangential motion of colloids trapped just at the nanoslot entrance becomes more pronounced with increased voltage. Nanocolloids larger than the nanoslot depth and weak electrolytes (0.1 m*M*) were used. Figure taken from Yossifon & Chang (2010). Abbreviations: EOF, electro-osmotic flow; EP, electrophoresis.

component becomes negative (**Figure 15*b***). This pressure-driven backflow in the microreservoir is responsible for the corner vortices with a vorticity direction parallel to the chip substrates. **Figure 15*c,d*** shows more explicit numerically computed streamlines for a simple model geometry of a nanoslot bounded by two microreservoirs. The occurrence of this corner vortex can be simply explained based on liquid flux continuity arguments.

As these vortices driven by electro-osmotic flow in the microchannel have a vorticitiy axis parallel to the width of the nanoslot, they are perpendicular to the vortices in **Figure 6** because of the vortex instability. **Figure 16** shows a nanocolloid suspension at the depleted entrance of a nanoslot first captured by the horizontal vortices at low voltages and then by the vertical vortex array due to instability at higher voltages, producing a complex toroidal pattern at the end. The figure also shows these dynamic nanocolloids trapping at the depleted side of a fluidic nanoslot entrance (Yossifon & Chang 2010) to sensitively regulate DC ion transport through the nanoslot such that a second limiting-overlimiting transition occurs in its nonlinear *I-V* characteristics. The transition from the corner vortex to a complex torus with both vortical motions coincides with

the first overlimiting transition, whereas electrostatic interaction of nanocolloids in these vortices with the nanoslot entrance drives the second limiting transition.

CONCLUDING REMARKS

It is counterintuitive that microvortices can appear at microfluidic scales and that these vortices can dramatically enhance current through ion-selective nanoslots and nanoporous membranes. We believe these vortices can remove filter cake and fouling on membranes and can enhance the efficiency of many ion-exchange and separation processes involving ion-selective membranes. When large and charged biomolecules such as nucleic acids hybridize onto a nanoslot or a nanoporous membrane, they can form a permselective monolayer such that the monolayer/nanoslot membrane becomes a bipolar membrane with new and distinct ion current dynamics. We hence believe that the large-voltage nonlinear phenomena involving hydrodynamics, combined with low-voltage rectification due to intrapore asymmetries, can lead to a new class of nonlinear nanofluidic circuits for very sensitive biosensing. In such circuits, nanofluidic diodes will be connected to nanofluidic oscillators, relays, and hysteretic elements to produce ion current networks not unlike those in neuronal networks. It is quite fortuitous that they also exhibit a rich spectrum of hydrodynamic and pattern-formation phenomena that are of interest to the fluid dynamics community.

SUMMARY POINTS

1. The microvortex instability of extended polarization has been verified. Also, convection by the instability produces a sharp increase in ion-selective membrane flux: the overlimiting current.

2. Hydrodynamic nanofluidic diodes can be designed with asymmetric microchannel and/or nanochannel entrance geometries.

3. Vortex dynamics involves classical subharmonic vortex coalescence.

4. The diffusion front dynamics during the establishment of the extended polarization allows simple universal scaling.

5. The depletion length that determines the overlimiting current is selected by an equilibrium vortex state.

6. External hydrodynamics is important to ion flux through nanochannels and ion-selective membranes.

FUTURE ISSUES

1. Investigators should focus on the exact mechanism for selecting the vortex equilibrium state and the depletion length scale for different entrance geometries—radially convergent/divergent vortices, microchamber height/width, and asymmetric ionic strengths.

2. The sensitivity of microvortex instability and the overlimiting current to membrane charge and morphologies should be studied.

3. The flux interaction among nanopores should be explored.

4. Researchers should work on developing hydrodynamic molecular sensors that are sensitive to molecular hybridization onto membranes.

5. An important topic is rectification inversion as the intrapore mechanism due to nanochannel asymmetry at low-voltage transitions to high-voltage external depletion mechanisms due to microchamber or nanochannel entrance asymmetry.

6. Molecular mixing, concentration, and separation using the depletion and microvortices should be explored.

7. Excitable, bistable, and oscillatory ion currents should be generated using, for example, bipolar membranes.

DISCLOSURE STATEMENT

ACKNOWLEDGMENTS

LITERATURE CITED

Balster J, Yildirim MH, Stamatialis DF, Ibanez R, Lammertink RG, et al. 2007. Morphology and micro-topology of cation-exchange polymers and the origin of limiting current. *J. Phys. Chem. B* 111:2152–65

Barany S, Mishchuk NA, Prieve DC. 1998. Superfast electrophoresis of conducting dispersed particles. *J. Colloid Interface Sci.* 207:240–50

Basuray S, Senapati S, Ajian A, Mahon AR, Chang H-C. 2009. Shear and AC field enhanced carbon nanotube impedance assay for rapid, sensitive and mismatch-discriminating DNA hybridization. *ACS Nano* 3:1823–30

Ben Y, Chang H-C. 2002. Nonlinear Smoluchowski slip velocity and micro-vortices. *J. Fluid Mech.* 461:229–38

Ben Y, Demkhin EA, Chang H-C. 2004. Superfast nonlinear electrokinetics and electrophoresis. *J. Colloid Interface Sci.* 276:483–97

Branton D, Deamer DW, Marziali A, Bayley H, Benne SA, et al. 2008. The potential and challenges of nanopore sequencing. *Nat. Biotechnol.* 26:1146–53

Chang H-C. 1994. Wave evolution on a falling film. *Annu. Rev. Fluid Mech.* 26:103–36

Chang H-C, Demekhin EA. 2002. *Complex Wave Dynamics on Thin Films*. Amsterdam: Elsevier Sci.

Chang H-C, Yossifon G. 2009. Understanding electrokinetics at the nanoscale: a perspective. *Biomicrofluidics* 3:012001

Chang H-C, Yeo LY. 2010. *Electrokinetically Driven Microfluidics and Nanofluidics*. Cambridge, UK Cambridge Univ. Press

Cheng L-J, Guo L-J. 2007. Rectified ionic transport through concentration gradient in homogeneous silica nanochannels. *Nano Lett.* 10:3165–71

Cheng L-J, Guo L-J. 2009. Ionic current rectification, breakdown and switching in heterogeneous oxide nanofluidic devices. *ACS Nano* 3:575–84

Cheng L-J, Guo L-J. 2010. Nanofluidic diodes. *Chem. Soc. Rev.* 39:923–38

Carried out matched asymptotics from the electroneutral region with the extended polarized region interfacing the ion-selective membrane.

Cheng IF, Senapati S, Cheng X, Basuray S, Chang H-C. 2010. A rapid field-use assay for mismatch number and location of hybridized DNAs. *Lab Chip* 10:828–31

Chetwani N, Maheshwari S, Chang H-C. 2008. Universal cone angle of AC electrosprays due to net charge entrainment. *Phys. Rev. Lett.* 101:204501

Craighead H. 2006. Future lab-on-a-chip technologies for interrogating individual molecules. *Nature* 442:387–93

Dekker C. 2007. Solid-state nanopores. *Nat. Nanotechnol.* 2:209–15

Demekhin EA, Shapar EM, Lapchenko VV. 2008. Initiation of electroconvection in semipermeable electric membranes. *Dokl. Phys.* 53:450–53

Dukhin SS. 1991. Electrokinetic phenomena of the second kind and their applications. *Adv. Colloid Interface Sci.* 35:173–96

Eastman JA, Choi SS, Li S, Yu W, Thompson LJ. 2001. Anomalously increased effective thermal conductivities of ethylene glycol–based nanofluids containing copper nanoparticles. *Appl. Phys. Lett.* 78:718–20

Hunter R. 1981. *Zeta Potential in Colloid Science: Principles and Applications.* New York: Academic

Jung JY, Joshi P, Petrossian L, Thornton TJ, Posner JD. 2009. Electromigration current rectification in a cylindrical nanopore due to asymmetric concentration polarization. *Anal. Chem.* 81:3128–33

Kalaidin E-N, Polyanskikh SV, Demekhin EA. 2010. Self-similar solutions in ion-exhange membranes and their stability. *Dokl. Phys.* 55:502–6

Karnik R, Duan C, Castelino K, Daiguji H, Majumdar A. 2007. Rectification of ionic current in a nanofluidic diode. *Nano Lett.* 7:547–51

Karnik R, Fan R, Yue M, Li D, Yang P, Majumdar A. 2005. Electrostatic control of ions and molecules in nanofluidic transistors. *Nano Lett.* 5:943–48

Keener J, Sneyd J. 1998. *Mathematical Physiology.* New York: Springer-Verlag

Kim D, Raj A, Zhu L, Maselb RI, Shannon MA. 2008. Non-equilibrium electrokinetic micro/nano fluidic mixer. *Lab Chip* 8:625–28

Kim SJ, Ko SH, Kang KH, Han J. 2010. Direct seawater desalination by ion concentration polarization. *Nat. Nanotechnol.* 5:297–301

Kim SJ, Wang YC, Lee JH, Jang H, Han J. 2007. Concentration polarization and nonlinear electrokinetic flow near a nanofluidic channel. *Phys. Rev. Lett.* 99:044501

Levich VG. 1962. *Physicochemical Hydrodynamics.* New York: Prentice Hall

Maletzki F, Rosler H-W, Staude E. 1992. Ion transfer across electrodialysis membranes in the overlimiting current range: stationary voltage current characteristics and current noise power spectra under different conditions of free convection. *J. Membr. Sci.* 71:105–15

Mani A, Zangle TA, Santiago JG. 2009. On the propagation of concentration polarization from microchannel-nanochannel interfaces. Part I: analytical model and characteristic analysis. *Langmuir* 25:3898–908

Mannion JT, Craighead HG. 2006. Nanofluidic structures for single biomolecule fluorescent detection. *Biopolymers* 85:131–43

Moffatt HK. 1964. Viscous and resistive eddies near a sharp corner. *J. Fluid Mech.* 18:1–18

Morrison FA. 1970. Electrophoresis of a particle of arbitrary shape. *J. Colloid Interface Sci.* 34:210–14

Pu Q, Yun J, Temkin P, Liu S. 2004. Ion-enrichment and ion-depletion effect of nanochannel structures. *Nano Lett.* 4:1099–103

Rubinstein I, Shtilman L. 1979. Voltage against current curves of cation exchange membranes. *J. Chem. Soc. Faraday Trans. II* 75:231–46

Rubinstein I, Zaltzman B. 2000. Electro-osmotically induced convection at a permselective membrane. *Phys. Rev. E* 62:2238–51

Rubinstein I, Zaltzman B, Pretz J, Linder C. 2002. Experimental verification of the electroosmotic mechanism of overlimiting conductance through a cation exchange electrodialysis membrane. *Russ. J. Electrochem.* 38:853–63

Rubinstein SM, Manukyan M, Staicu A, Rubinstein I, Zaltzman B, et al. 2008. Direct observation of a nonequilibrium electro-osmotic instability. *Phys. Rev. Lett.* 101:236101

Stein D, Kruithof M, Dekker C. 2004. Surface-charge-governed ion transport in nanofluidic channel. *Phys. Rev. Lett.* 93:035901

Demonstrated a rectification current effect in the overlimiting region across a nanopore connecting asymmetric chambers.

Simulated the self-similar evolution of the depletion front and the resulting vortex merging dynamics.

Experimentally verified the overlimiting-current behavior and the existence of a vortex in fabricated nanochannels.

First postulated that this potential singularity must be smoothed by an extended polarized region that matches the electroneutral fundamental solution of the diffusion equation.

First predicted theoretically/numerically the microvortex instability mechanism at ion-selective nanoporous membranes.

First experimentally verified, using ion-selective membranes, the vortex instability and its connection to the overlimiting current.

Takhistov P, Indeikina A, Chang H-C. 2002. Electrokinetic displacement of air bubbles in microchannels. *Phys. Fluids* 14:1–14

Taylor GI. 1964. Disintegration of water drops in an electric field. *Proc. R. Soc. A* 280:383–97

Thamida SK, Chang H-C. 2002. Nonlinear electrokinetic ejection and entrainment due to polarization at nearly insulated wedges. *Phys. Fluids* 14:4315–28

Van Der Heyden FHJ, Bonthuis DJ, Stein D, Meyer C, Dekker C. 2006. Electrokinetic energy conversion efficiency in nanofluidic channels. *Nano Lett.* 6:2232–37

Van Der Heyden FHJ, Stein D, Dekker C. 2005. Streaming currents in a single nanofluidic channel. *Phys. Rev. Lett.* 95:116104

Vlassiouk I, Siwy ZS. 2007. Nanofluidic diode. *Nano Lett.* 7:552–56

Wang P, Chen Z, Chang H-C. 2006. A new electro-osmotic pump based on silica monoliths. *Sensors Actuators B* 113:500–9

Wang S-C, Wei H-H, Chen H-P, Tsai M-H, Yu C-C, Chang H-C. 2008. Dynamic superconcentration at critical-point double-layer gates of conducting nanoporous granules due to asymmetric tangential fluxes. *Biomicrofluidics* 2:014102

Yossifon G, Chang H-C. 2008. Selection of non-equilibrium over-limiting currents: universal depletion layer formation dynamics and vortex instability. *Phys. Rev. Lett.* 101:254501

Yossifon G, Chang H-C. 2010. Changing nanoslot ion flux with a dynamic nanocolloid ion-selective filter: secondary overlimiting currents due to nanocolloid-nanoslot interaction. *Phys. Rev. E* 81:066317

Yossifon G, Chang Y-C, Chang H-C. 2009a. Rectification, gating voltage and interchannel communication of nanoslot arrays due to asymmetric entrance space charge polarization. *Phys. Rev. Lett.* 103:154502

Yossifon G, Frankel I, Miloh T. 2006. On electro-osmotic flows through micro-channel junctions. *Phys. Fluids* 18:117108

Yossifon G, Mushenheim P, Chang H-C. 2010a. Controlling the nanoslot overlimiting current by varying the micro-chamber depth. *Eur. Phys. Lett.* 90:64004–9

Yossifon G, Mushenheim P, Chang H-C. 2010b. Eliminating the limiting-current phenomenon by geometric field focusing into nanopores and nanoslots. *Phys. Rev. E* 81:046301

Yossifon G, Mushenheim P, Chang Y-C, Chang H-C. 2009b. Nonlinear current-voltage characteristics of nano-channels. *Phys. Rev. E* 79:046305

Zangle TA, Mani A, Santiago JG. 2009. On the propagation of concentration polarization from microchannel-nanochannel interfaces. Part II: numerical and experimental study. *Langmuir* 25:3909–16

First experimentally verified, using a fabricated nanochannel, the depletion front, the vortex instability and their connection to the overlimiting current.

First presented evidence of interchannel communication of a nanoslot array on the overlimiting current.

Along with Yossifon et al. 2010b, controlled the vortex instability onset and overlimiting current by varying the nanoslot width and the height of a microchamber connected to the nanoslot.

RELATED RESOURCES

Prof. Chang's website: **http://www.nd.edu/~changlab/**
Dr. Yossifon's website: **http://mnfl.technion.ac.il/**